Distributed measurement and modified Navier-Stokes model of gas pressure profile evolution in hollow-core antiresonant fibres

Elizaveta Elistratova , Thomas W. Kelly, Ian A. Davidson, Hesham Sakr, Thomas D. Bradley, Austin Taranta, Francesco Poletti, Radan Slavík, Peter Horak, and Natalie V. Wheeler

Abstract—Recent progress in reducing the loss of hollow-core fibres (HCFs) makes them great candidates for many fibre applications. However, as the fibre's optical properties depend on the gas pressure and composition within the core and cladding holes, it is essential to understand the gas dynamics at play when the fibres are pressurised, vented or evacuated. Here, we investigate the gas flow dynamics along the core of an HCF with a more complex microstructure design, as is typical of recent state-of-the-art HCFs. We use a novel distributed technique based on optical time-domain reflectometry (OTDR). This technique enables measurement of the evolution of the pressure distribution within the hollow core during the gas-filling process over long fibre lengths. Using these results, we show that the pressure distribution inside the HCF can be simulated using simplified Navier-Stokes equations and approximating the fibre core as a simple cylindrical tube of ~ 0.7 times the fibre core diameter.

Index Terms—Hollow-core fibres, pressure profile, GDRI, gas filling, gas flow, optical time-domain reflectometry

I. Introduction

HOLLOW-CORE antiresonant fibres (HC-ARFs), such as nested antiresonant nodeless fibres (NANFs) and double nested antiresonant nodeless fibres (DNANFs), are state-of-the-art HCFs which combine the usual benefits of HCFs such as low nonlinearity, low dispersion, high damage threshold, near-vacuum speed of light [1] with a record low loss [2], [3]. These fibres are being deployed in various applications [4], and both control and long-term stability of their optical properties are becoming increasingly important. Here, the gas within the core and cladding regions of the fibre plays an important role.

When an HCF has been left with unsealed ends for a long time, it is expected to have the same gas content at the same pressure as the surrounding atmosphere. In normal conditions, the internal gas composition would be air containing water vapour and other possible contaminants (such as hydrogen chloride gas [5]) at atmospheric pressure. However, for standard fabrication processes, the starting condition for an HCF internal volume is not atmospheric pressure air and thus an understanding of the time-scales and conditions required for gas-content equalisation is needed. A recent study showed [6] that as-drawn HC-ARFs (fibres whose ends are sealed immediately after fabrication) have an internal pressure significantly lower than atmospheric, close to ~ 0.2 bar, principally due to the temperature drop ($\sim 2000°C$) between the fibre in the

All authors are with Optoelectronics Research Centre, University of Southampton, UK.

furnace and the final fibre combined with the extreme change in hole size during the fibre draw. Upon opening the fibre ends to the atmosphere, the pressure gradient pushes atmospheric air inside, consequently creating a temporary pressure gradient along the fibre until full equalisation with the surrounding atmosphere has occurred.

Due to the possibility of contaminants entering the HCF's microstructure [7], and hence degradation of their optical properties, sealing or enclosing the fibre ends is a strategy which can be employed successfully. However, such fibres must still be unsealed for further testing, use, or system integration. It has been demonstrated that unsealing the fibre ends and initiating a pressure equalisation process affects fibre transmission properties [8]. As an HC-ARF's core is usually larger than the capillaries forming the cladding, and the gas travels faster through a larger capillary, core pressure rises faster to atmospheric than the cladding pressure. This creates a transient core-cladding pressure gradient that is termed gas-induced differential refractive index (GDRI) [9], which temporarily improves the fibre transmission properties. This could affect the loss measurements of HC-ARFs, in which confinement loss is the dominant loss mechanism, if they are carried out while the core and cladding pressures are equalising.

Understanding the time periods involved in this process, and opening up the possibility of exploiting the GDRI to improve the fibre properties, relies on understanding the gas dynamics inside the fibre; these control fibre filling and venting times. Initially, the gas-filling dynamics were studied using early HCF designs, where the core can be closely approximated by a circular tube [10], [11]. In this case, an analytical model can be derived to predict the pressure profile evolving inside the fibre. However, as was shown in [12], a circular tube approximation does not work well for recent HC-ARFs due to a more complex core shape (see a cross-section of the fibre used in this work in Fig. 1). Using numerical modelling, it was demonstrated that the circular tube model is insufficient to obtain simulation results consistent with the gas flow measurements for such fibre geometries. Along with a flow velocity maximum at the fibre core, local velocity maxima were observed in the gaps between capillaries. Such a phenomenon resulted in a lower overall mean velocity in the fibre than in a fibre-core-sized tube.

Previous works studied the gas dynamics inside HCFs by averaging methods, specifically using absorption spectroscopy

[8], [9], [10], [12]. Such methods allow the average gas concentration inside the fibre to be measured but not the pressure distribution and its evolution over time. To measure gas pressure or density distribution we would need to capture how light is interacting with a segment dz along the fibre's length. Such a measurement is possible with OTDR.

In OTDR the fibre is characterised by measuring a backscatter signal from each point along the length of the fibre. This technique is routinely used with traditional solid-core fibres to locate breakages and imperfections [13]. In HC-ARFs, backscattering comes from three contributors [14]: the Rayleigh backscattering from the bulk glass, backscattering caused by surface roughness of the glass surface, and backscattering from the gas inside the fibre core. At atmospheric pressure, the glass and surface roughness contributions to backscatter for typical HC-ARF designs are more than an order of magnitude lower than that of the gas [14]. Therefore, applying the OTDR technique to HC-ARFs can provide information on the gas distribution inside the fibre. Although backscattering from atmospheric air within an HC-ARF is around 30 dB lower than from silica in the core of a solid-core fibre, commercially available OTDR instruments have been shown to produce measurable signals [13] if the issue of strong back-reflection is carefully addressed.

Here, we demonstrate this novel experimental technique and use it to measure the pressure profile of the gas inside the core region of a NANF along the fibre length, while the fibre is being filled with gas (or vented). We use these measurements to further investigate the application of the cylindrical tube model [10] for more complex HC-ARF structures, such as NANFs. Based on the comparison between the experimental and simulation results, we propose introducing a correction factor - an effective diameter coefficient - that allows us to simulate the pressure distribution inside the core and predict fibre filling and venting times (as the time to pressure profile stabilisation) using the simple tube model. The reported general technique will be fully applicable to other HCF designs not presented here (such as the "ice-cream cone" type [15]) but potentially with slight modification.

In this paper, details of the fibre under test are presented in Section II. The cylindrical tube model used to simulate the gas flow dynamics inside the HCF is described in Section III. The experimental setup for distributed measurements of the gas pressure evolution using OTDR is described in Section IV and the results of the experiments, model comparison and the model correction factor are presented in Section V.

II. STRUCTURAL AND OPTICAL PROPERTIES OF THE FIBRE

The fibre used here is a NANF [2], as shown in Fig. 1. The fibre's core is defined by 5 capillaries (outer capillaries) with a nested capillary (inner capillary) inside each. The fibre core diameter D_c is 35 μm, the average outer capillary diameter is 37.1 μm with average thickness of 0.44 μm, the average inner capillary diameter is 18.9 μm with average thickness of 0.39 μm, and the gaps between outer capillaries are on average 5.7 μm.

The fibre was designed for C-band operation in its first antiresonant window [2] with a measured loss of 0.30 ± 0.06
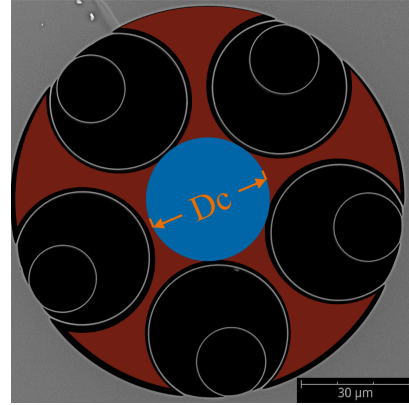

Fig. 1: SEM image of the NANF used in this work. Red: "extended" fibre core area. Blue: fibre core area, and area of the tube model, where $D = D_c$.

dB/km at 1550 nm. The loss of the fibre is close to the loss of standard telecom fibre.

The length of the fibre sample in this study was chosen as $L = 435$ m; this is considerably longer than fibres used in previous reports of gas flow dynamics in HCFs (typically lengths of 15 m or less have been investigated) and approaches the fibre lengths used for some telecommunication applications while keeping the experiment timescales manageable (gas filling time scales with the square of the fibre length, see Section III). The fibre was left exposed to the atmosphere post-fabrication prior to our experiments for over a year. Therefore, the initial conditions within the fibre's microstructure were expected to be similar to atmospheric conditions.

III. GAS FLOW MODEL

The flowing air inside the core of the NANF can be modelled using the time-dependent laminar compressible Navier-Stokes equations (for an in-depth explanation see Appendix A).

It was shown in [10] and [16], that the Navier-Stokes equations can be simplified to get a single equation for an approximated pressure distribution inside of a cylindrical tube. So, by replacing the complex shape of the fibre core with a simple tube of diameter D we get an approximated pressure distribution inside of a fibre:

$$\frac{\partial p}{\partial t} = \frac{D^2}{32\mu} \frac{\partial}{\partial z} \left[p \frac{\partial p}{\partial z} \right], \qquad (1)$$

where p is pressure, μ is dynamic viscosity of the gas, t is time, and z is the spatial coordinate along the fibre length. We will refer to Eq. (1) as the tube model in the remainder of the paper.

Applying $\partial p / \partial t = 0$ and boundary conditions $p(z = 0) = P_0$ (pressure at the proximal end of the fibre) and $p(z = L) = P_L$ (pressure at the distal end of the fibre), we get the steady-state solution

$$p_s(z) = \sqrt{P_0^2 - \frac{z}{L} (P_0^2 - P_L^2)}, \qquad (2)$$
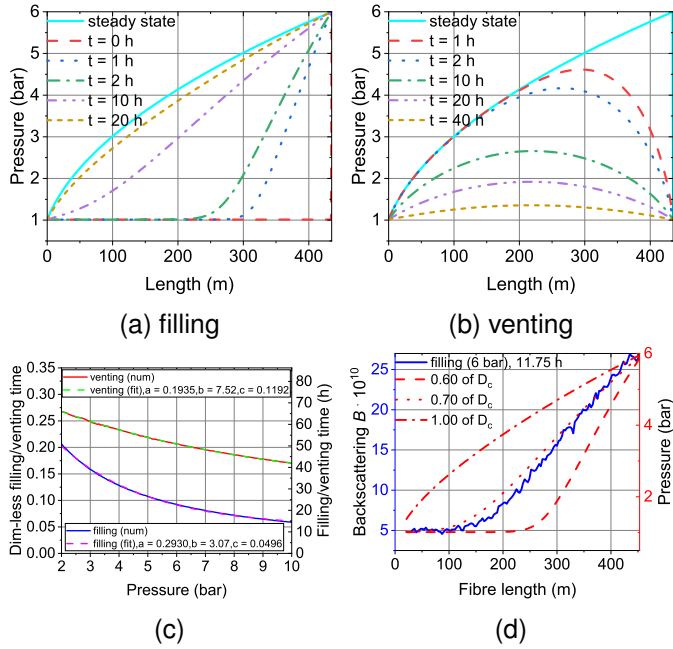
where L is the fibre length.

Fig. 2: Numerical solutions of the tube model pressure equation (Eq. (1)) for an air-filled tube with a 35 μm hole diameter, a 453 m length and initial internal gas pressure of 1 bar: (a) filling/pressurizing from the distal end with a 6 bar pressure source and the proximal end open to atmosphere, (b) post-fill venting (outlets of both fibre ends at 1 bar), (c) numerically calculated values of filling and venting times for different filling pressures along with their fits with fitting parameters a, b, and c. (d) Example of fitting pressure curves for various D_{eff} (red) to a backscatter curve (blue). Shown for the case of 11.75 hours after beginning pressurising air-filled NANF at 6 bar pressure from its distal end.

Numerical solutions of Eq. (1) are shown in Fig. 2 for the following scenario: a fibre (cylindrical tube with core diameter D_c), which has an initial uniform pressure distribution of 1 bar along its length, is filled from its distal end ($z = L$) with air at $P_L = 6$ bar while the proximal end ($z = 0$) is kept open to atmospheric air (at $P_0 = 1$ bar) (Fig. 2a) and subsequently vented by removing the pressure source at the distal end (Fig. 2b).

During the process of filling, the gas pressure front gradually moves from the distal to the opposite (proximal) end, eventually taking the shape of the steady-state solution in Eq. (2). The venting process starts with the distal end of the steady-state solution dropping to atmospheric pressure and the pressure profile across the fibre evolving by flattening to an even pressure distribution.

Filling and venting times

We define the filling time as the time elapsed from when the pressure is applied to the distal end until the length-average pressure inside the fibre core reaches 95% of its maximum (the average pressure of the steady-state). Similarly, the venting time was defined as the time taken till the average pressure inside the fibre core reaches 5% above its minimum (1 bar).

As can be seen in Fig. 2a, the maximum average pressure inside the fibre is reached when the pressure distribution has reached a steady state after > 20 hours. While in general the value of averaged pressure alone does not guarantee that the shape of the pressure distribution is indeed a steady state in the experiment, this is essentially checked by fitting the model to the experiment in section V(b). The levels of 95% (and 5%) were chosen as they are sufficiently high (low) to more closely match the steady-state profile both in the model and the experiment but not too high (low) to introduce additional uncertainty due to rapid (fall) of the averaged pressure and normalised backscattering function for filling (venting).

To define filling/venting time as a function of the filling pressure P, the dimensionless counterpart of Eq. (1) was solved for a range of pressures $P = 2..10$ bar:

$$\frac{\partial \overline{p}}{\partial \overline{t}} = \frac{\partial}{\partial \overline{z}} \left[\overline{p} \frac{\partial \overline{p}}{\partial \overline{z}} \right], \tag{3}$$

where $\overline{p} = p/P_a$, $\overline{z} = z/L$, $\overline{t} = t/K_h$, and $K_h = \frac{32\mu L^2}{D^2 P_a}$, P_a is the atmospheric pressure.

The results of the computation are shown in Fig. 2c with solid blue and red lines for filling and venting respectively. Both filling and venting times closely approximate an exponential dependence on pressure so the equation $y = a \exp(-P/b) + c$ was fitted to them. The fitted curves have a very good agreement with the numerical data as can be seen in Fig. 2c (dashed magenta and green lines for filling and venting respectively). Then, the functions for dimensional filling and venting times (obtained by multiplying the fitted curves by K_h) of pressure $P = 2..10$ bar are:

$$T_{fil} = \frac{32\mu L^2}{D^2 P_a} \left[0.2930 \cdot \exp\left(-\frac{P}{3.07} + 0.0496 \right) \right], \tag{4}$$

$$T_{ven} = \frac{32\mu L^2}{D^2 P_a} \left[0.1935 \cdot \exp\left(-\frac{P}{7.52} + 0.1192 \right) \right]. \tag{5}$$

As can be seen in Fig. 2c, the dimensionless filling time remains about 0.1 units lower than the venting times throughout the range of pressures from 3 to 10 bar closing that gap by about a half between 2 and 3 bar.

Thus, the average difference between the filling and venting time is

$$T_{fil} - T_{ven} \approx 0.1 \cdot \frac{32\mu L^2}{D^2 P_a} = \frac{3.2\mu L^2}{D_c^2 P_a} \tag{6}$$

making the average difference between the filling and venting time of a tube with diameter $D = 35 \mu$m and length $L = 435$ m with air: $T_{fil} - T_{ven} \approx 22.6$ hours.

Eqs. (4)-(6) should be valid for a range of μ, L, D and P as long as the flow is in hydrodynamic regime, laminar and compressible (see Appendix A). Thus, the filling and venting times would increase with the viscosity of gas μ and square of the tube length-to-diameter ratio (L/D_c), and decrease exponentially with the applied pressure P.

For a tube of 35 μm diameter and 435 m length, which approximates our NANF, the filling and venting times $T^t_{fill/vent)}$ calculated by Eq. (4) and (5) for 3, 4.5, and 6 bar filling pressure are presented in Table I.

TABLE I: Filling and venting times evaluated from the experiment and model, and effective diameter coefficient calculated based on their values.

|	$T^{exp}_{fill/vent)}$, h	$T^{t}_{fill/vent)}$, h	k_{eff} (prediction)	k_{eff} (fitting)
6 bar (fil.)	48.42	10.75	0.47	0.70
6 bar (ven.)	70.17	24.20	0.59	0.70
4.5 bar (fil.)	58.82	17.52	0.55	0.70
4.5 bar (ven.)	123.95	29.54	0.49	0.75
3 bar (fil.)	45.15	28.57	0.80	0.75
3 bar (ven.)	245.15	36.06	0.38	0.70

Fig. 3: (a) Experimental setup for measuring the pressure distribution dynamic inside NANF via OTDR by filling the fibre with gas from one end and subsequently venting. (b) Typical backscatter power traces recorded by the OTDR. Shown for the case of filling NANF with air at 6 bar from the distal end.

IV. EXPERIMENTAL SETUP

In order to measure the evolution of the longitudinal pressure profile along the core of the NANF, we used a novel approach based on OTDR. The setup was based on a commercial OTDR (LOR-200, Luciol Instruments S.A.) to measure the localised scattering (and hence pressure) in an HCF, as shown in Fig. 3a. One of the key challenges here is minimising end face reflections, so OTDR pulses at 1550 nm were delivered to the NANF by a solid-core fibre with an 8°-angle-polished mode-matching adapter and a simple four-layer anti-reflective coating [13]. The solid-core fibre was carefully butt-coupled to the NANF using a 5d alignment stage (xyz and pitch and yaw). The mode-matching adapter at the end of the solid-core fibre enlarged the diameter of the mode field to match that of the NANF's fundamental mode. Since the solid-core fibre and NANF were not spliced, the space between them allowed for the gas to exit the fibre, keeping this end of the fibre at atmospheric pressure. The NANF was wound on a bobbin ~ 318 mm in diameter, though we do not expect that typical coiling diameters (> 100 mm diameter) have an effect on filling/venting time. The distal end of the NANF was secured in a custom gas pressure chamber attached to a pressure gauge [9]. To fill the fibre, dry air was supplied through the gas line to the pressure chamber. After filling, the fibre was subsequently vented. For venting the fibre was not removed from the gas chamber. To bring the gas chamber end of the fibre to atmospheric pressure, the gas supply was cut off and the valve (V1 in Fig. 3a) on the gas chamber was opened. The OTDR pulses delivered to the NANF scatter from the gas inside the fibre and the backscattered portion was captured through the same delivery solid-core fibre and processed in the OTDR unit.

The width of OTDR pulses was set at 100 ns to achieve a high enough signal-to-noise ratio and fibre length resolution. With this setup, we were able to measure backscattered signals from a NANF filled with air at atmospheric pressure that were 10 dB above the noise floor and a fibre length resolution of 15 m.

An active auto-alignment system (Nanotrac, Thorlabs) was installed to maintain the coupling over long periods (over a week). The Nanotrac system monitored the fibre throughput power changes via a photodiode (D in Fig. 3a) placed behind the gas chamber window. If the throughput power dropped, the
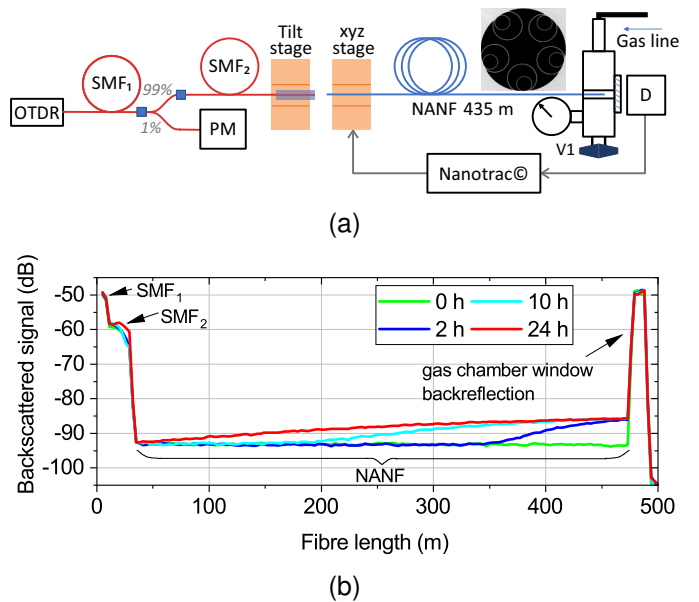
Nanotrac controller acted to move the piezoelectric drivers in the XYZ stage to re-align the fibres and return the throughput power to its original level. The throughput power was recorded via a custom Labview script and used for the normalisation of the backscatter signal. For the same purpose, the OTDR power was recorded through a 1 % splitter channel (power meter PM in Fig. 3a).

The described setup produced the backscatter traces shown in Fig. 3b. Here, the NANF was filled with dry air at 6 bar pressure from its distal end. The double reflection peak at the beginning of the trace marked the splice between SMF$_1$ and SMF$_2$, and the coupling to NANF. The peak at the end of the trace was due to the remaining distal end-face back-reflection and gas chamber window. In between the peaks lies the backscatter signal from the gas inside NANF. As the gas pressure front moves further into the fibre, the backscatter signal rises due to the increased gas density in a manner akin to the pressure distributions given by the tube model (Fig. 2a). Generally, a change in gas composition would also be reflected in the backscatter signal. However, here the fibre is both pre-filled and pressurised with air, so all changes to the backscatter signal are only due to density (pressure) changes

The experiments were performed in the following order: 6 bar filling, 6 bar venting, 4.5 bar filling, 4.5 bar venting, 3 bar filling, 3 bar venting. As can be seen from that order, the fibre was vented in between each filling experiment, that is, the fibre was left until its internal pressure had returned to 1 bar/atmospheric pressure. This return to 1 bar was determined by the venting experiment continuing until the observed backscattering distribution did not significantly change over a

time period of several hours as can be seen in Fig. 4d.

Backscatter data processing

Considering an OTDR measurement of a fibre with a backscatter coefficient B, the power P_{bsc} reflected from a 1-m length section of fibre situated a distance z away from the launch end of the fibre is given by [13]

$$P_{bsc}(z,t) = P_{in}\eta(t)B(z,t)e^{(-2\alpha z)}, \tag{7}$$

where $P_{in} = \langle P_{in}\rangle \beta(t)$ is the OTDR output power [1] with an average over time power $\langle P_{in}\rangle$ and fluctuations $\beta(t)$, α is the NANF's attenuation, and $\eta(t)$ is the fibre coupling coefficient, which may fluctuate in time t due to the misalignment of the 5d stage.

The OTDR records the attenuation of the sent pulse power in dB/m, $10\log\left(\frac{P_{bsc}(z)}{P_{in}^0}\right)$, where P_{in}^0 is the value of the OTDR output power recorded into OTDR memory during calibration. The fibre throughput power is

$$P_{thr}(t) = \langle P_{in}\rangle \beta(t)\eta(t)e^{(-\alpha L)}. \tag{8}$$

Substituting Eq. (8) into Eq. (7), converting it to dB/m, and assuming $P_{in}^0 = \langle P_{in}\rangle$, the backscatter coefficient $B(z,t)$ in dB/m is:

$$10\log\left(B(z,t)\right) = 10\log\left(\frac{P_{bsc}}{\langle P_{in}\rangle \beta(t)\eta(t)e^{(-2\alpha z)}}\right) =$$
$$10\log\left(\frac{P_{bsc}(z)}{\langle P_{in}\rangle}\right) - 10\log\left(\frac{P_{thr}(t)e^{(\alpha(L-2z))}}{\langle P_{in}\rangle}\right), \tag{9}$$

Therefore, we can obtain the backscatter $B(z,t)$ by "normalising" the backscatter signal by the fibre throughput power, average OTDR power and fibre loss contribution.

Note that we use a simplification by not considering the dependence of fibre loss on the pressure inside the core [9]. Thus, a GDRI contribution to the backscatter signal will still be present in the processed data.

V. RESULTS AND DISCUSSION

A. Gas pressure distribution maps

The NANF was filled and subsequently vented three times at different filing pressures 3, 4.5, and 6 bar through its distal end. Backscatter traces were recorded continuously (~ 1 trace per 2 minutes over several days) until the pressure profile stabilised. The backscatter signal's evolution for filling and venting at 6 bar is shown in Fig. 4a and 4d respectively in the form of time/fibre length heatmaps (heatmaps for 3 and 4.5 bar can be found in Appendix B).

The filling and venting times were evaluated in the same way as for the tube model. The evolution of the average pressure in the fibre is represented in Fig. 4g and 4h by the backscattering integrated over fibre length and normalised to its value in the last backscatter trace recorded. Despite normalising the data, some fluctuations remained, so an exponential

---

[1]Commercial OTDRs, such as the one used in this experiment, often record data in terms of signal amplitude rather than optical power. Here, we talk about data already converted to optical power.

---

function was fitted to find at which time 95 % and 5 % of relative backscattering were reached for filling and venting respectively. Values of filling and venting times $T_{fill/vent}^{exp}$ obtained this way for all experiments are presented in Table I.

Experimental filling and venting times differ significantly from those obtained in simulations for a fibre-core-sized cylindrical tube. It suggests that a tube diameter $D_{eff} \neq D_c$ should be used in the model to correctly predict the filling/venting time. We define an effective diameter coefficient k_{eff} as the ratio of effective diameter D_{eff} to fibre core diameter D_c. Using the filling/venting time's connection to the diameter of the tube D, we find

$$k_{eff} = \frac{D_{eff}}{D_c} = \sqrt{\frac{T_{fill/vent}^t}{T_{fill/vent}^{eff}}}, \tag{10}$$

where $T_{fill/vent}^t$ is the filling or venting time of the tube of D_c diameter and $T_{fill/vent}^{eff}$ is the filling or venting time of the tube of diameter D_{eff}. There is no difference between using only filling or only venting times to calculate k_{eff}, both options provide the same value.

Then, substituting $T_{fill/vent}^{eff}$ for values of experimental filling and venting times in Eq. (10), we predicted the effective diameter coefficient for each experiment. As only the filling pressure changed from one experiment to the other, there should be minimal deviation of its values for all of the six experiments. However, as we can see in Table I, the values of the predicted effective diameter coefficient span from 0.38 to 0.80. We attribute this fact to an imperfect method of obtaining experimental filling and venting times: as the normalised backscattering functions in Fig. 4g and 4h possess significant noise in some cases, the values can have large error bars. So fitting of the tube model was used as described in the next section.

B. Fitting to the OTDR trace procedure

An obvious (and simple) way to apply the described model is to approximate the complex fibre structure with the tube of the fibre core diameter (blue-shaded region in Fig. 1). However, some flow will likely occur in the gaps between capillaries (red-shaded region in Fig. 1) and this will influence the overall filling rate. According to Eqs. (4) and (5), the filling and venting times depend inversely on the area. Since the area of the "extended" core (core + gaps) is larger than the core alone, we could expect a decrease in filling/venting time compared to the model. Yet, the flow through the narrowest parts of the gap will be slower (due to the smaller cross-sectional area compared to the core region) than the rest of the fibre, which might indicate an overall increase in filling/venting time compared to the model. This corroborates that a tube diameter $D_{eff} \neq D_c$ should be used in the model to correctly predict the filling/venting time.

To investigate this dynamic, the tube model was fitted to the experimental results. As the tube model does not have an analytical solution, we cannot directly fit it to the data. So, to determine which D_{eff} best fits the experiment, the
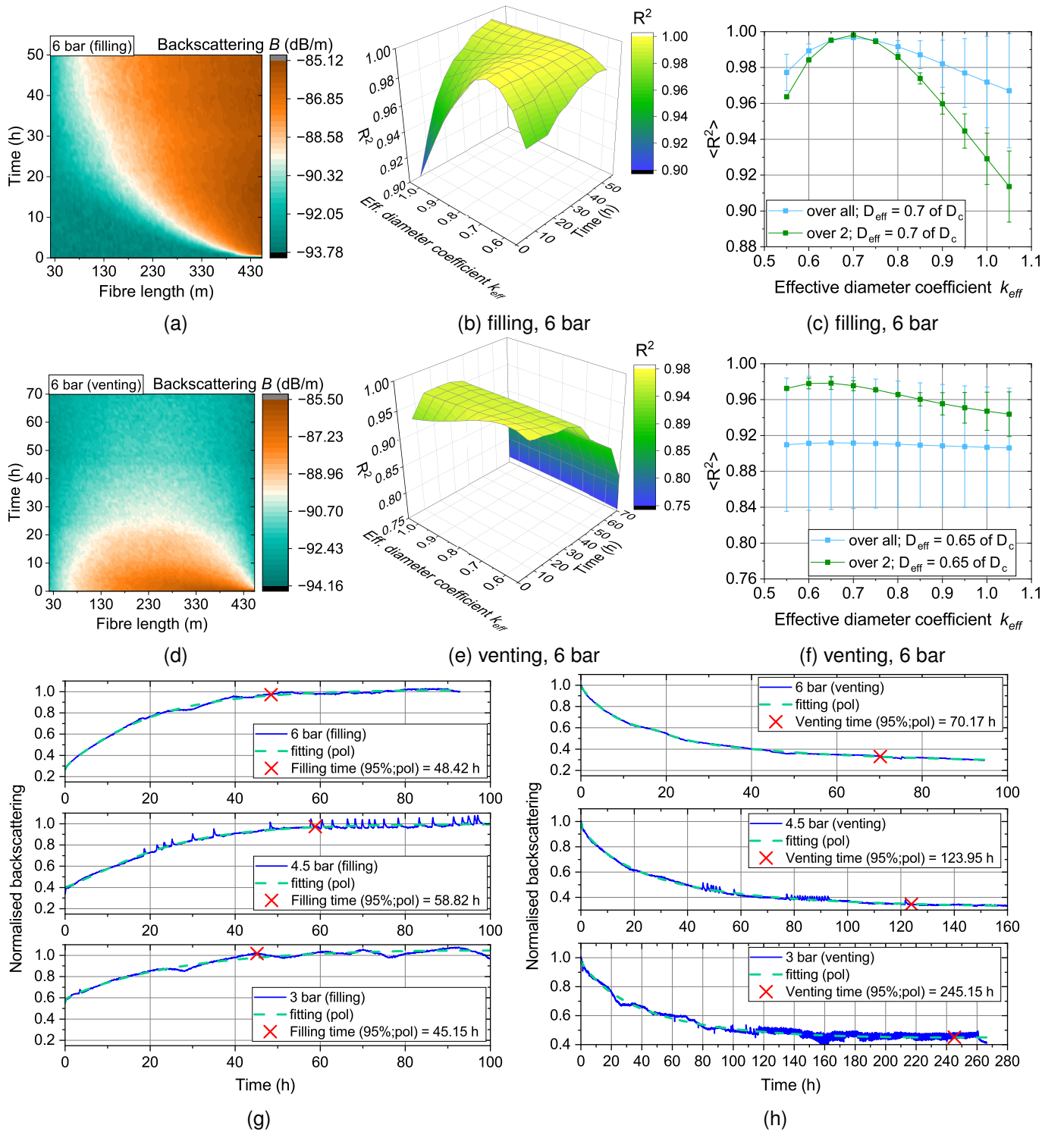
Fig. 4: Heat maps showing backscattering from the moving pressure front for filling (a) NANF with air at 6 bar and subsequently venting (d). Values of R^2 for fitting the tube model at various D_{eff} to the experimental backscatter data at 6 bar filling pressure: (b,c) for 10 time steps from the beginning of the experiment to filling/venting time $T_{fill/vent}^{exp}$; (e,f) averaged over a whole range of time steps (cyan) and two first time steps (green). Calculated relative backscattering functions for filling at 6, 4.5, and 3 bar pressure (g) and venting (h), and their fits. The crosses show when the functions for filling (venting) grow (drop) by 95 % which determines the filling (venting) time.

tube model (Eq. (1)) was solved for a range of $D_{eff,i} = (0.55, 0.60, ..., 1.05)D_c$ and $t_i = (0, 0.1, ..., 1)T_{fill/vent}^{exp}$ re- sulting in an array of pressure curves $p(z, t_i; D_{eff,i})$. Since the optical width of the OTDR pulse resulted in a 15 m fibre- length resolution of the backscatter data, the pressure solutions

were convolved with a square pulse of 15 m width. Three such pressure curves are shown in Fig. 2d with red lines for the case of filling the fibre with 6 bar pressure 11.75 hours after the beginning of the experiment.

Since the backscatter coefficient is a linear function of pressure [17], both pressure solutions and backscatter data were normalised and a least-squares fit was performed. In the following section, we visualise the fitting results by plotting the values of the coefficient of determination R^2.

C. Effective diameter and time coefficients

The fitting procedure was performed for each of the six experiments. Obtained values of R^2 at 6 bar are shown in Fig. 4b and 4c for filling, and Fig. 4e and 4f for venting (R^2 graphs for 3 and 4.5 bar can be found in Appendix B). Fig. 4b and 4e show values of R^2 for different k_{eff} at different times into the filling and venting processes. We do not include values of R^2 at $t = 0$ regardless of k_{eff} because the pressure distribution would be the same for all of them: for filling it is a uniform distribution of atmospheric pressure, for venting a steady-state solution (Eq. (2)). In Fig. 4c and 4f, the values of R^2 are averaged over the whole time range (cyan curve) or only two time steps (green curve).

For filling, the values of R^2 reach almost 1 for a certain effective diameter coefficient k_{eff}, indicating that the pressure distribution of the fibre can be well approximated with a tube model across all times (from the beginning of the filling to the steady-state). Eventually all values of R^2 for different k_{eff} reach a maximum of ~ 1 as the steady-state pressure distribution is the same for all tube diameters (Eq. (2)). Therefore, the first hours of the experiment are most representative of a particular structure and what k_{eff} should be used for it in the tube model. That is also confirmed by obtaining the same maximum at $k_{eff} = 0.70 - 0.75$ for each case averaging over the whole range of times and only over the first two time steps (out of 10 considered).

For venting, we find similar trends, but also we see a rapid degradation of the fit at later times as R^2 drops below 0.9, which we believe is due to the relative OTDR noise increasing at lower backscatter values. Nevertheless, the maximum of R^2 stays almost the same when averaging over the whole time range or just two time steps at $k_{eff} = 0.70 - 0.75$.

Combining all optimum values of k_{eff} for all six cases we get $k_{eff} = 0.72 \pm 0.03$, meaning that the time-dependence of the pressure distribution in the fibre core is described by that of the tube of a diameter reduced by 0.72 times or of a surface reduced by $k_{eff}^2 = 0.52$ times. Therefore, the pressure front inside of the fibre core moves $1/0.52 = 1.93$ times slower than would be expected of a tube with the same size, as

$$T_{fil} \sim \frac{1}{D_{eff}^2} \sim \frac{1}{A_{eff}}, \qquad (11)$$

where A_{eff} is the area that is being filled.

The slowing of the process in the fibre compared to the tube was also shown in [12] by numerically solving the full Navier-Stokes equations. We attribute this to slower gas filling in the smaller voids within the complex cladding structure which leads to gas being pushed along the fibre in the core but subsequently leaking through the gaps between the capillaries to fill the whole available cross-section of the HC-ARF.

Thus, the ratio of the "extended" core area A_{c+g} (core + gaps) to the core surface area should tell us by how much the filling time should increase (or the pressure front should slow down). However, such a ratio for our NANF equals 3.57, which is significantly larger than the value of 1.93 we obtained through fitting. It might mean that the transverse gas flow through the gaps is significantly slowed by the gap size and the longitudinal flow in the interstitials. Since the area of each individual gap is smaller than the area of the core, the flow in the gaps must fall behind the flow in the core. Such a difference in filling dynamic might be another reason for a decline in fit quality with time. Different filling times of the core and capillaries would also create a GDRI that would introduce a varying loss along the fibre, and the tube model does not account for that loss.

VI. Conclusion

We have presented a novel method for measuring the distributed gas pressure evolution in the core of an HCF. This method uses a commercial OTDR system, in combination with carefully designed coupling optics to minimize reflections, to measure backscattering from the gas within the fibre. This is possible in an HCF because scattering from other contributions (e.g. Rayleigh scattering by the glass) is substantially lower. Key advantages of this approach, apart from the distributed measurement, are the ability to measure the pressure evolution in long fibres with high time resolution. This enabled the capture of experimental data that we have compared with a gas flow model which assumes a cylindrical fibre core. We showed that the gas flow inside a NANF exists in a hydrodynamic regime and can be well simulated using the Navier-Stokes equations, when approximating the fibre's complex core structure with an "effective" cylindrical tube. Such an approach allows for a quick estimation of fibre's filling and venting times, which are important when considering fibre equalisation to the atmosphere or a sealed fibre break. For the NANF studied here, the cylindrical tube has to have a diameter of ~ 0.7 of the fibre's core diameter. This NANF design, including the core size and gaps, is reasonably representative of current state-of-the-art fibres designed for low loss in the C-band. However, for fibres designed for different wavelengths, or as fibre designs evolve, further investigations will be necessary to understand how this effective core diameter changes with fibre structure. Neither the tube model nor the OTDR method allow us to look at the gas dynamics past the fibre's core and at the volumetric flow rates inside the whole structure, and thus full numerical simulations of the 3-dimensional Navier-Stokes equations may be required for a more detailed analysis.

VII. Acknowledgements

access, the authors have applied a Creative Commons attribution license (CC BY) to any Author Accepted Manuscript version arising from this submission.

VIII. DATA AVAILABILITY

The data for this paper is available at https://doi.org/10.5258/SOTON/D2982.

APPENDIX A
NAVIER-STOKES EQUATIONS

In general, gas flow can be considered as a flow composed of individual discrete particles (molecular regime) or as a macroscopic continuous fluid flow (hydrodynamic regime) [17]. The choice of a regime is determined by the *Knudsen* number $Kn \equiv \lambda_{fp}/l$, where λ_{fp} is the mean free path between inter-molecular collisions, and l is the characteristic dimension of the fibre [12], with a Knudsen number of $\ll 1$ representing continuous flow and $\gg 1$ molecular flow (and the regime between corresponding slip/transitional flow). Inserting the formula for the mean free path λ_{fp} [10] into the equation for the *Knudsen* number we get: $Kn = \frac{k_B T}{\sqrt{2}\pi d^2 p_0 l}$, where k_B is the Boltzmann constant, T is the temperature, d is the kinetic diameter of the gas molecule, and p_0 is the characteristic pressure.

The hydrodynamic regime is governed by the Navier-Stokes equations (as we show in the following section the gas flow in NANF is hydrodynamic based on the *Knudsen* number calculation). The Navier-Stokes equations are partial differential equations that describe the motion of a fluid. They consist of conservation of mass and conservation of momentum Eqs. (12, 13) [2]

$$\frac{\partial \overline{\rho}}{\partial t} + \nabla \cdot (\rho \overline{\mathbf{u}}) = 0, \tag{12}$$

$$\overline{\rho}\frac{D\overline{\mathbf{u}}}{Dt} = -Eu\nabla\overline{p} + \frac{1}{Fr^2}\overline{\rho}\,\overline{g} + \frac{1}{Re}\left[\nabla^2\overline{\mathbf{u}} + \frac{1}{3}\nabla(\nabla\cdot\overline{\mathbf{u}})\right], \tag{13}$$

where $\frac{D}{Dt}$ is the total time derivative, ρ is the fluid's density, $\mathbf{u}$ is the fluid's velocity, p is the pressure, g is the gravitational acceleration, and μ is the fluid's dynamic viscosity.

Eqs. (12) and (13) are presented in their dimensionless form, where each variable is normalised by its characteristic value u_0, p_0, ρ_0, g_0, x_0. This allows us to evaluate the contribution of each term in Eq. (13) and simplify it by considering three parameters: the *Euler* number $Eu = \frac{p_0}{\rho_0 u_0^2}$, the *Reynolds* number $Re = \frac{\rho_0 u_0 x_0}{\mu}$, and the *Froude* number $Fr = \frac{u_0}{\sqrt{g_0 x_0}}$ [17]. Another useful simplification can be made by estimating the compressibility of the flow. For *incompressible* flow, the density of the fluid particles (small fluid volumes) does not change but different fluid particles may have different densities [17]. Generally, the compressibility of the flow is determined by the *Mach* number $M = \frac{u_0}{c_s}$, where c_s is a speed of sound. It has been noted [12], [18] that the *Mach* number alone is not enough to determine incompressibility of the flow inside

TABLE II: Range of dimensionless parameters and modified incompressibility criterion for pressures of 3 and 6 bar.

p_0 bar	ρ_0, kg/m^3	u_0, m/s	Kn $\cdot 10^3$	Eu $\cdot 10^4$	Re	Fr $\cdot 10^2$	M $\cdot 10^3$	Mod. crit.
3	3.57	5.3	3.5	3	36	8.1	1.5	81
6	7.13	13.2	17	0.5	181	20.2	3.9	101

of a long narrow channel (such as the NANF or any other HCF). For this case, a modified incompressibility criterion was suggested in [12]: $\frac{L}{D_c}\frac{M^2}{Re} \ll 1$, where L is the fibre length, and D_c is the fibre core.

The values of Kn, Eu, Re, Fr, M, and the modified compressibility criterion for our experiment are evaluated in Table II. For air particles with $d = 4.19 \cdot 10^{-10}$ m and a pressure range $p_0 = 3...6$ bar, we get $Kn = 0.035...0.017 \ll 1$. Therefore, our flow is in the hydrodynamic regime and we can safely use the Navier-Stokes equations. To evaluate Eu, Re, Fr, and Ma, we set characteristic flow parameters: u_0 is calculated as average velocity in pressure-driven, steady, laminar flow; ρ_0 is calculated at $T = 273$ K [19] (values for u_0 and ρ_0 are given for pressures (3, 6) bar in Table II), for the *Froude* number $x_0 = 435$ m (fibre length), for the *Reynolds* number $x_0 = 35$ μm (fibre core), air viscosity $\mu = 1.82 \cdot 10^{-5}$ kg/(m · s) [19], and gravitational acceleration $g_0 = 9.8$ m/s^2.

As can be seen from Table II, the *Froude* number takes significantly smaller values than Eu and Re, therefore, the gravity term can be dropped from Eq. (13). At values of Re exceeding 2300, the flow transitions from *laminar* to *turbulent* (in *laminar* flow, the fluid is moving in parallel layers with no unsteady macroscopic mixing or overturning motion of the layers [17]. Turbulent flow describes the opposite scenario and requires a modified approach in combination with the Navier-Stokes equations. As here the *Reynolds* number takes values lower than 2300, the flow can be considered *laminar*. Values of the modified incompressibility criterion are significantly higher than 1, therefore, we have to treat the flow as compressible.

---

[2]In the most general case viscosity μ depends on the spatial coordinates and cannot be taken out of the divergence term in the conservation of momentum equation, and temperature should be included in the $\rho - p$ relationship. Here, we assume the viscosity and temperature to be constant.

APPENDIX B
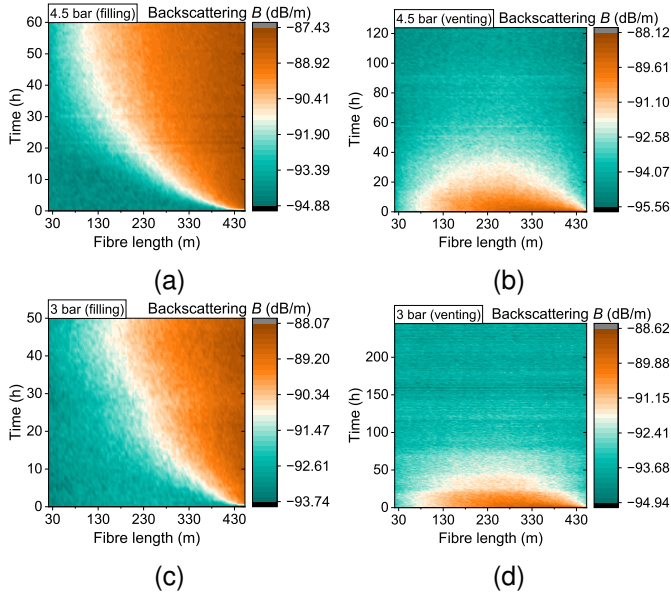### FIGURES FOR 3 AND 4.5 BAR FILLING EXPERIMENTS

Fig. 5: Heat maps showing backscattering from the moving pressure front for filling NANF with air at 4.5 and 3 bar (a,c) and subsequently venting (b,d).
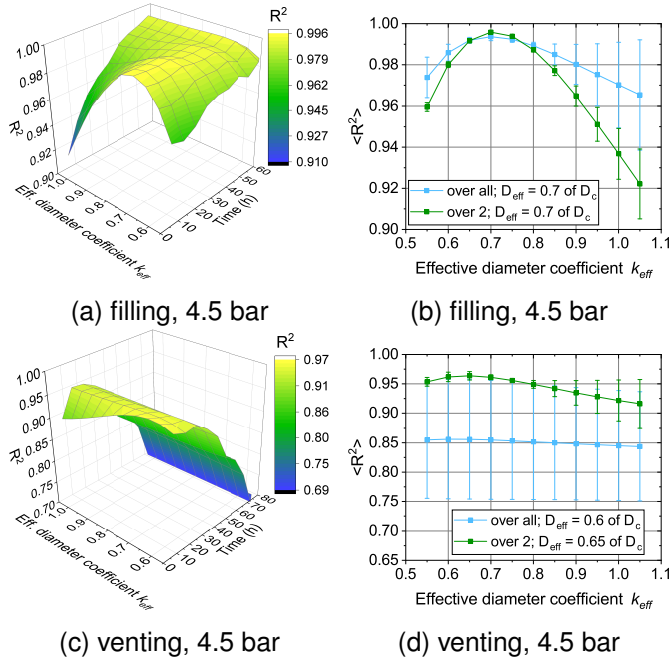

Fig. 6: Values of R^2 for fitting the tube model at various D_{eff} to the experimental backscatter data at 4.5 bar filling pressure: (a,c) for 10 time steps from the beginning of the experiment to filling/venting time $T^{exp}_{fill/vent}$; (b,d) averaged over a whole range of time steps (cyan) and two first time steps (green).
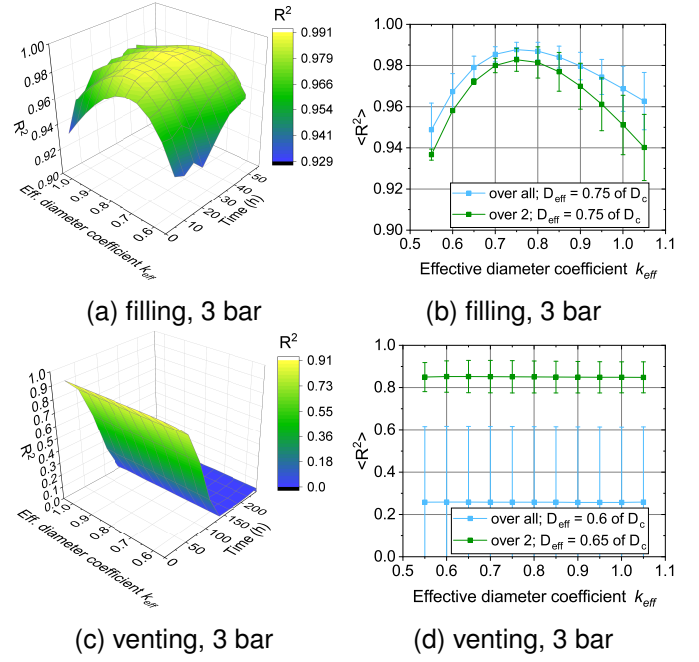

Fig. 7: Values of R^2 for fitting the tube model at various D_{eff} to the experimental backscatter data at 3 bar filling pressure: (a,c) for 10 time steps from the beginning of the experiment to filling/venting time $T^{exp}_{fill/vent}$; (b,d) averaged over a whole range of time steps (cyan) and two first time steps (green).

REFERENCES

[1] P. S. J. Russell, P. Hölzer, W. Chang, A. Abdolvand, and J. C. Travers, "Hollow-core photonic crystal fibres for gas-based nonlinear optics," *Nature Photonics*, vol. 8, pp. 278–286, Apr. 2014.

[2] H. Sakr, T. D. Bradley, G. T. Jasion, E. N. Fokoua, S. R. Sandoghchi, I. A. Davidson, A. Taranta, G. Guerra, W. Shere, Y. Chen, J. R. Hayes, D. J. Richardson, and F. Poletti, "Hollow Core NANFs with Five Nested Tubes and Record Low Loss at 850, 1060, 1300 and 1625nm," in *Optical Fiber Communication Conference (OFC) 2021*, (Washington, DC), p. F3A.4, Optica Publishing Group, 2021.

[3] G. T. Jasion, H. Sakr, J. R. Hayes, S. R. Sandoghchi, L. Hooper, E. N. Fokoua, A. Saljoghei, H. C. Mulvad, M. Alonso, A. Taranta, T. D. Bradley, I. A. Davidson, Y. Chen, D. J. Richardson, and F. Poletti, "0.174 dB/km Hollow Core Double Nested Antiresonant Nodeless Fiber (DNANF)," in *Optical Fiber Communication Conference (OFC) 2022*, (San Diego, California), p. Th4C.7, Optica Publishing Group, 2022.

[4] A. Iqbal, P. Wright, N. Parkin, M. Fake, M. Alonso, S. R. Sandoghchi, and A. Lord, "First Demonstration of 400ZR DWDM Transmission through Field Deployable Hollow-Core-Fibre Cable," in *Optical Fiber Communication Conference (OFC) 2021*, (Washington, DC), p. F4C.2, Optica Publishing Group, 2021.

[5] N. V. Wheeler, M. N. Petrovich, N. K. Baddela, J. R. Hayes, E. N. Fokoua, F. Poletti, and D. J. Richardson, "Gas Absorption between 1.8 and 2.1 μm in Low Loss (5.2 dB/km) HC-PBGF," in *Conference on Lasers and Electro-Optics 2012*, (San Jose, California), p. CM3N.5, OSA, 2012.

[6] S. Rikimi, Y. Chen, M. C. Partridge, I. A. Davidson, G. T. Jasion, T. D. Bradley, A. A. Taranta, F. Poletti, M. N. Petrovich, D. J. Richardson, and N. V. Wheeler, "Pressure in As-drawn Hollow Core Fibers," in *OSA Advanced Photonics Congress (AP) 2020 (IPR, NP, NOMA, Networks, PVLED, PSC, SPPCom, SOF)*, (Washington, DC), p. SoW1H.4, OSA, 2020.

[7] S. Rikimi, Y. Chen, T. W. Kelly, I. A. Davidson, G. T. Jasion, M. Partridge, K. Harrington, T. D. Bradley, A. A. Taranta, F. Poletti, M. N. Petrovich, D. J. Richardson, and N. V. Wheeler, "Internal Gas Composition and Pressure in As-drawn Hollow Core Optical Fibers," *Journal of Lightwave Technology*, vol. 40, pp. 4776–4785, July 2022.

[8] S. Rikimi, T. W. Kelly, P. Horak, Y. Chen, I. A. Davidson, S. Bawn, T. D. Bradley, A. A. Taranta, F. Poletti, D. J. Richardson, and N. V.

Wheeler, "Transient differential pressure-induced loss variation in as-drawn hollow core optical fibres," in *Micro-Structured and Specialty Optical Fibres VII* (C.-A. Bunge, K. Kalli, and P. Peterka, eds.), (Strasbourg, France), p. 2, SPIE, May 2022.

[9] T. W. Kelly, P. Horak, I. A. Davidson, M. Partridge, G. T. Jasion, S. Rikimi, A. Taranta, D. J. Richardson, F. Poletti, and N. V. Wheeler, "Gas-induced differential refractive index enhanced guidance in hollow-core optical fibers," *Optica*, vol. 8, p. 916, June 2021.

[10] J. Henningsen and J. Hald, "Dynamics of gas flow in hollow core photonic bandgap fibers," *Applied Optics*, vol. 47, p. 2790, May 2008.

[11] R. Wynne and B. Barabadi, "Gas-filling dynamics of a hollow-core photonic bandgap fiber for nonvacuum conditions," *Applied Optics*, vol. 54, p. 1751, Mar. 2015.

[12] P. Bojeś, P. Jaworski, K. Krzempek, Z. Malecha, F. Yu, D. Wu, P. Kozioł, G. Dudzik, M. Liao, and K. Abramski, "Experimental and numerical analysis of gas flow in nodeless antiresonant hollow-core fibers for optimization of laser gas spectroscopy sensors," *Optics & Laser Technology*, vol. 152, p. 108157, Aug. 2022.

[13] R. Slavík, E. R. Numkam Fokoua, T. D. Bradley, A. A. Taranta, M. Komanec, S. Zvánovec, V. Michaud-Belleau, F. Poletti, and D. J. Richardson, "Optical time domain backscattering of antiresonant hollow core fibers," *Optics Express*, vol. 30, p. 31310, Aug. 2022.

[14] E. Numkam Fokoua, V. Michaud-Belleau, J. Genest, R. Slavík, and F. Poletti, "Theoretical analysis of backscattering in hollow-core antiresonant fibers," *APL Photonics*, vol. 6, p. 096106, Sept. 2021.

[15] F. Yu, W. J. Wadsworth, and J. C. Knight, "Low loss silica hollow core fibers for 3–4 um spectral region," *Optics Express*, vol. 20, p. 11153, May 2012.

[16] E. Arkilic, M. Schmidt, and K. Breuer, "Gaseous slip flow in long microchannels," *Journal of Microelectromechanical Systems*, vol. 6, pp. 167–178, June 1997.

[17] P. K. Kundu, I. M. Cohen, and D. R. Dowling, *Fluid Mechanics*. Elsevier, 6th ed., 2016.

[18] C. C. Wong, T. L. Zoeller, D. R. Adkins, and J. N. Shadid, "Ivestigation of gas flow in long and narrow channels," in *FEDSM00-11314, Proceedings of ASME 2000 Fluid Engineering Division Summer Meeting*, 2000.

[19] "The Engineering ToolBox." https://www.engineeringtoolbox.com/.

Hesham Sakr Hesham Sakr is an Optical Engineer at Microsoft, UK, specialising in developing hollow core fibres for Microsoft Azure Fibre. Before joining Microsoft, Hesham was a postdoc researcher at the ORC, Southampton, focusing on developing ultralow loss and ultrawide band HCFs, suitable for applications including optical telecoms and high-power delivery. The work led to multiple Nature and postdeadline OFC publications. Hesham received his BEng and PhD from the University of Nottingham, UK. Currently, Hesham serves as a committee member in Optica's Optical Fabrication and Testing early career group and is part of the D5 sub-committee of the Optical Fibre Communications Conference (OFC).

Thomas D. Bradley Dr Thomas Bradley is currently an assistant professor in the High Capacity Optical Transmission lab in the Electro-Optics Communication (ECO) group at Eindhoven University of Technology. His current research focuses on the application of novel optical fibres and fibre devices to quantum and classical sensing and high-capacity data transmission. His PhD and earlier career research has focused on the fabrication, characterisation and quantum optics experiments gas filled antiresonant and photonic bandgap hollow core fibers. He received an MPhys degree in 2009 and a PhD degree in 2014 from the University of Bath, UK. Between 2014 and 2021 he worked at the Optoelectronics Research Centre (ORC), University of Southampton as a research fellow and senior research fellow in the micro-structured optical fibre group, where he led the fabrication of world record-breaking Nested Anti-resonant Nodeless Fibers (NANFs). In 2014 he was awarded the best early career presentation prize at the EPSRC Manufacturing the Future conference. He is a senior member of the OPTICA Society (formally OSA).

Elizaveta Elistratova Elizaveta received her master's degree in Optical Engineering in Moscow in 2020 from Bauman Moscow State University. Her Hollow-core Fibre research began at the Photonics and IR Technology Centre in collaboration with the Fibre Optics Research Centre during her degree, investigating fibre bend loss and polarisation properties. In 2021 she received the Corning Women in Optical Communications Scholarship. The same year she was accepted to a PhD position at the Optoelectronics Research Centre, University of Southampton, UK. Currently, she is working towards her thesis on gas effects in hollow-core fibres, supervised by Dr Natalie Wheeler.

Austin Taranta Austin Taranta received the B.Sc. in Chemical Engineering from the Massachusetts Institute of Technology in 2006. From 2006 to 2016, Austin was an Optical Engineer at Honeywell Aerospace focusing on the design and manufacture of high-performance fibre-optic gyroscopes for defence and space applications. Austin joined the Optoelectronics Research Centre at the University of Southampton in 2016 as a member of the technical staff. His current research focuses on novel solid and hollow core fibre sensors, and polarization properties of hollow core antiresonant fibres. He holds several patents and has authored or co-authored more than 40 peer-reviewed publications.

Thomas W. Kelly Thomas W. Kelly received the M.Phys. degree from the University of Southampton, Southampton, U.K., in 2019. His research focuses on using hollow core fibres for Raman gas phase spectroscopy.

Ian A. Davidson Ian A. Davidson received his BSc degree (in physics) from the University of Edinburgh in 2004, and an MSc degree in photonics and optoelectronic devices from the Universities of St. Andrews and Heriot-Watt in 2007. His PhD degree was awarded by Heriot-Watt University in 2013, where he worked on the growth, processing, and characterization of II-VI semiconductor materials. He joined the Optoelectronics Research Centre at the University of Southampton as a research fellow in 2017 and was promoted to senior research fellow in January 2022, having previously undertaken post-doctoral research work at Heriot-Watt (2012-13) and Stockholm (2013-2017) Universities. His current research work focuses on the fabrication and characterisation of micro-structured optical fibres.

Francesco Poletti Francesco Poletti received the Laurea degree in electronics engineering from the University of Parma, Parma, Italy, and the Ph.D. degree from the Optoelectronics Research Centre (ORC), Southampton, U.K., in 2000 and 2007, respectively. He is currently a Professor at the ORC. He has worked for three years on optical network design at Marconi Communications and for more than 15 years on the development of new generations of microstructured optical fibers at the ORC. His research interests include the design of antiresonant hollow core optical fibers, the development of fiber-optic characterization techniques, and the fabrication of silica as well as non-silica-based fibers and devices.

Radan Slavik Radan Slavík (M'07–SM'07) received the M.Sc. and Ph.D. degrees in optics and optoelectronics from the Faculty of Mathematics and Physics, Charles University, Prague, Czechia, in 1996 and 2000, respectively, and the D.Sc. degree from the Academy of Sciences of the Czech Republic in 2009. In 1995–2000 and 2004–2009, he was with the Institute of Photonics and Electronics, Czech Academy of Sciences, Prague, Czechia. In 2000– 2003, he was with the Centre d'Optique, Photonique et Laser, Université Laval, QC, Canada, as a Postdoctoral Research Fellow. Since 2009, he has been with the Optoelectronics Research Centre, University of Southampton, U.K. His research interests include optical and optics-assisted signal processing, the study of environmental sensitivity of optical fibres and hollow core optical fibres and their applications in telecommunications, metrology, and sensing. He is a Fellow member of the OPTICA and a Senior member of IEEE.

Peter Horak Peter Horak received the M.Sc. degree in theoretical physics and the Ph.D. degree in theoretical quantum optics from the University of Innsbruck, Innsbruck, Austria, in 1993 and 1997, respectively. Since 2001, he has been with the Optoelectronics Research Centre, University of Southampton, U.K., where he is currently an Associate Professor and heads the Computational Nonlinear Optics group. His research interests include the theoretical and numerical investigation of photonic devices, including optical fibres and planar platforms, as well as linear, nonlinear, and quantum optical effects.

Natalie V. Wheeler Dr Natalie Wheeler is a Principal Research Fellow at the Optoelectronics Research Centre (ORC), University of Southampton, U.K. Dr Wheeler has worked on the fabrication and applications of hollow core fibres (HCFs) for > 15 years and led the fabrication of many state-of-the-art HCFs which have been used in world-leading demonstrations across diverse applications, including telecoms, high power laser delivery and high sensitivity gas detection. She was awarded a prestigious Royal Society University Research Fellowship (2015-2025) and leads ORC activities on gas-filled HCFs, including active control of the gas content within HCFs post-fabrication for applications including control of HCF optical properties, gas sensing and metrology and investigations into the long term lifetime and reliability of HCFs. She has co-authored > 190 publications, including ~ 40 invited/post-deadline papers.